

Photodissociation and Photoionization Mechanisms in Lanthanide-based Fluorinated β -Diketonate Metal–Organic Chemical-Vapor Deposition Precursors

Qingguo Meng, Robert J. Witte, P. Stanley May, and Mary T. Berry*

Department of Chemistry, University of South Dakota, Vermillion, South Dakota 57069

Received July 27, 2009. Revised Manuscript Received October 16, 2009

A detailed photodissociation mechanism for the fluorinated lanthanide (Ln) β -diketonate metal–organic chemical-vapor deposition (MOCVD) precursors Ln(fod)₃, Ln(hfac)₃, and Ln(hfac)₃diglyme was elucidated using photoionization time-of-flight mass spectrometry. The collisionless environment of the molecular beam source revealed a series of unimolecular steps, starting with dissociation of an intact β -diketonate ligand. Dissociation steps for the second and third ligands are associated with the attachment of a fluoride to the metal ion, leading to one of three ultimate products: Ln, LnF, or LnF₂. Except in the case of Pr, no LnO is observed. The pattern of ligand fragmentation strongly supports a mechanism for the fluoride-attachment step which is similar to one previously proposed for the thermally activated decomposition of Ce(hfac)₃glyme.¹ The detailed mechanistic understanding of the step-by-step fluorination will provide a basis for new ligand design, which maintains the advantageous mass-transport properties of the fluorinated precursors while controlling LnF_x formation.

Introduction

Understanding the photochemistry of gas-phase metal–organic compounds is fundamental to harnessing the full potential of laser-assisted metal–organic chemical-vapor deposition (L-MOCVD or LCVD), which can produce superior films, with finer grain boundaries and improved purity, as compared to traditional thermal activation techniques.^{2–5} Another advantage of LCVD over traditional thermal techniques is the potential for deposition on a wider range of substrates, including materials with poor thermal conductivity, or materials which cannot withstand elevated temperatures.⁶ LCVD technology has broad practical applications, including direct-write technology;⁷ deposition of amorphous carbon (α -C) films;⁸ carbon nanotubes;^{9,10} W, Mo, and V

films;¹¹ TiN films;¹² TiO₂ films;⁶ W nanoparticles;¹³ N-rich GaN_{1-x}P_x films and single quantum wells;^{14,15} N-rich GaInNP multiple quantum well structures;¹⁶ and polycrystalline Si solar cell applications.⁵

There is a great potential for the development of LCVD of lanthanide materials. Lanthanide oxides, fluorides, and nitrides, for example, have tremendously wide applications. Lanthanide oxides and, to a lesser extent, fluorides constitute the most important classes of industrial phosphors, Eu(III), Tb(III), and Eu(II) forming the most prevalent red/green/blue (RGB) phosphors, Nd(III) being the basis of the near infrared (NIR) phosphor in Nd:YAG lasers, and Er(III) providing the 1.55 μ m optical communication wavelength. Several lanthanide oxides, along with HfO₂, are currently the best candidates for alternative high-dielectric-constant gate oxides, which are urgently needed to replace the traditional SiO₂ gate dielectric as transistor size continues to shrink.^{17,18} In yet another example, the lanthanide oxides, Ln₂O₃, with appropriate defect structure, hold promise as the catalytic solution for methane conversion to liquid hydrocarbons.^{19–21}

*E-mail: mary.berry@usd.edu.

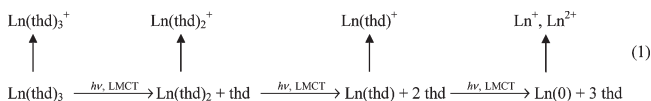
- (1) Pollard, K. D.; Jenkins, H. A.; Puddephatt, R. J. *Chem. Mater.* **2000**, *12*, 701.
- (2) Wexler, D.; Zink, J. I.; Tutt, L. W.; Lunt, S. R. *J. Phys. Chem.* **1993**, *97*, 13563.
- (3) Rutkowski, P. X.; Zink, J. I. *Inorg. Chem.* **2009**, *48*, 1655.
- (4) Tyndall, G. W.; Hacker, N. P. *Chem. Mater.* **1994**, *6*, 1982.
- (5) Sala, D. D.; Loreti, S.; Fornarini, L.; Menicucci, I.; Santoni, A.; Veneri, P. D.; Minarini, C.; Privato, C.; Lanconico, J. *Thin Solid Films*. **2002**, *403 & 404*, 302.
- (6) Halary-Wagner, E.; Wagner, F.; Hoffmann, P. *J. Electrochem. Soc.* **2004**, *151*, C571.
- (7) Boutros, K. S.; Roberts, J. C.; Bedair, S. M. *Appl. Phys. Lett.* **1996**, *68*, 2041.
- (8) Hukka, T. I.; Zhang, J. *J. Phys. Chem. B* **2000**, *104*, 7115.
- (9) Bondi, S. N.; Lackey, W. J.; Johnson, R. W.; Wang, X.; Wang, Z. L. *Carbon* **2006**, *44*, 1393.
- (10) Shi, J.; Lu, Y. F.; Yi, K. J.; Lin, Y. S.; Liou, S. H.; Hou, J. B.; Wang, X. W. *Appl. Phys. Lett.* **2006**, *89*, 083105.
- (11) Turney, W.; Hung, Y. M.; Starcevic, S. G.; Cardinahl, P. S.; Grassian, V. H.; Singmaster, K. A. *Chem. Mater.* **1992**, *4*, 1192.
- (12) Ishihara, S.; Hanabusa, M. *J. Appl. Phys.* **1998**, *84*, 596.

- (13) Landström, L.; Lu, J.; Hesler, P. *J. Phys. Chem. B* **2003**, *107*, 11615.
- (14) Kikawa, J.; Yoshida, S.; Itoh, Y. *J. Cryst. Growth*. **2001**, *229*, 48.
- (15) Kikawa, J.; Yoshida, S.; Itoh, Y. *Solid-State Electron.* **2003**, *47*, 523.
- (16) Yoshida, S.; Li, J.; Itoh, Y. *Phys. Stat. Sol. (c)* **2003**, *7*, 2236.
- (17) Jones, A. C.; Aspinall, H. C.; Chalker, P. R.; Potter, R. J.; Kukli, K.; Rahtu, A.; Ritala, M.; Leskelä, M. *J. Mater. Chem.* **2004**, *14*, 3101.
- (18) Gordon, R. G.; Becker, J.; Hausmann, D.; Suh, S. *Chem. Mater.* **2001**, *13*, 2463.
- (19) Lin, C. H.; Campbell, K. D.; Wang, J. X.; Lunsford, J. H. *J. Phys. Chem.* **1986**, *90*, 534.
- (20) Campbell, K. D.; Zhang, H.; Lunsford, J. H. *J. Phys. Chem.* **1988**, *92*, 750.
- (21) Podkolzin, S. G.; Stangland, E. E.; Jones, M. E.; Peringer, E.; Lercher, J. A. *J. Am. Chem. Soc.* **2007**, *129*, 2569.

Given the breadth of technologically important applications for inorganic lanthanide materials, and the advantages of LCVD in terms of clean, conformal, and potentially patterned deposition on a wide variety of substrates, it is important to investigate, and ultimately control, the photochemical mechanisms which convert the metal-organic precursor to the inorganic products of interest.

β -Diketonate complexes are traditional precursors for thermal MOCVD of lanthanide materials. Complexes of $\text{Ln}(\text{thd})_3$ ($\text{thd}^- = 2,2,6,6\text{-tetramethyl-3,5-heptanedionate}$) were first prepared and characterized by Sievers et al. in the 1960s.²² Precursors with fluorinated ligands, hexafluoroacetylacetonate (hfac^-) and 1,1,1,2,2,3,3-heptafluoro-7,7-dimethyl-4,6-octanedionate (fod^-), were shown to have more favorable characteristics of volatility and thermal stability.^{23,24} An even greater improvement in the mass transport characteristics was found for $\text{Ln}(\text{hfac})_3$ complexes, which included a polyether adduct, like $\text{Ln}(\text{hfac})_3\text{diglyme}$.^{1,25}

In previous work,^{26–28} we showed that photoionization mass spectrometry could be employed to elucidate the mechanism for photofragmentation of $\text{Ln}(\text{thd})_3$ leading to gas-phase production of both reduced metal species and metal oxide. A ligand dissociation mechanism was proposed which involved photoexcitation of a ligand-to-metal charge-transfer (LMCT) state in a vibronic transition to the repulsive wall of the LMCT state, well above the dissociation limit. LMCT excitation then results in dissociation of a neutral thd^* radical from the reduced Ln ion. Three sequential steps of LMCT excitation, each followed by ligand dissociation, lead to production of gas-phase $\text{Ln}(0)$, which is subsequently detected by mass spectrometry following postdissociation photoionization. This mechanism is illustrated in eq 1 below. The first step, in which $\text{Ln}(\text{thd})_2^+$ forms in competition with photoionization of the parent to form $\text{Ln}(\text{thd})_3^+$, is also illustrated in the potential energy diagram of Figure 1. Evidence to support this mechanism included observation of the $\text{Ln}(\text{thd})_n^+$ fragments and observation of a $\text{Eu}(0)$ ($^8\text{S}_{7/2} - ^8\text{P}_j$) signature in the resonance-enhanced multiphoton ionization (REMPI) spectrum of $\text{Eu}(\text{I})$.



Giuffrida et al.²⁹ also invoked a similar LMCT process in the photoreduction of ethanolic $\text{Cu}(\text{acac})_2$, producing

- (22) Eisentraut, K. J.; Sievers, R. E. *J. Am. Chem. Soc.* **1965**, *87*, 5254.
 (23) Richardson, M. F.; Wagner, W. F.; Sands, D. E. *J. Inorg. Nucl. Chem.* **1968**, *30*, 1275.
 (24) Springer, C. S., Jr.; Meek, D. W.; Sievers, R. E. *Inorg. Chem.* **1967**, *6*, 1105.
 (25) Malandrino, G.; Incontro, O.; Castelli, F.; Fragalà, I. L.; Benelli, C. *Chem. Mater.* **1996**, *8*, 1292.
 (26) Nelson, B. N.; Caster, A. G.; Berry, M. T. *Chem. Phys. Lett.* **2004**, *396*, 256.
 (27) Ow, F. P.; Berry, M. T.; May, P. S.; Zink, J. I. *J. Phys. Chem. A* **2007**, *111*, 4144.
 (28) Ow, F. P.; Berry, M. T.; May, P. S.; Zink, J. I. *J. Phys. Chem. A* **2006**, *110*, 7751.
 (29) Giuffrida, S.; Condorelli, G. G.; Costanzo, L. L.; Fragalà, I. L.; Ventimiglia, G.; Vecchio, G. *Chem. Mater.* **2004**, *16*, 1260.

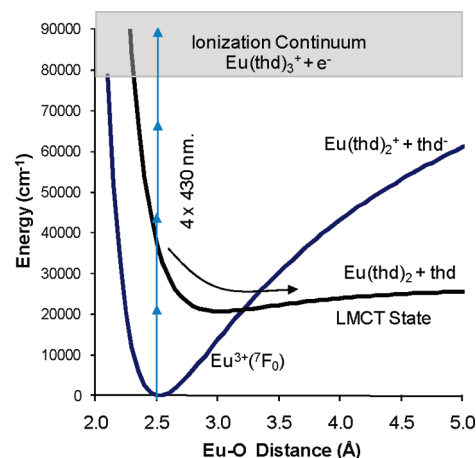


Figure 1. Potential energy diagram illustrating multiphoton ionization of the $\text{Eu}(\text{thd})_3$ parent molecule in competition with photofragmentation of the parent into the neutral fragments, $\text{Eu}(\text{thd})_2$ and thd , through interaction with an excited ligand-to-metal charge-transfer (LMCT) state. The $\text{Eu}(\text{thd})_2$ fragment may be observed by TOF-MS following multiphoton photoionization to $\text{Eu}(\text{thd})_2^+$.

deposits of metallic copper, though the mechanism in that instance is more complex, involving participation of the solvent (ethanol) and an acetone sensitizer.

As discussed above, the fluorinated precursors have superior transport properties. They are also excellent candidates for deposition of lanthanide fluorides.^{25,30} However, both $\text{Ln}(\text{hfac})_3$ and $\text{Ln}(\text{fod})_3$ require a co-precursor and postdeposition treatment in order to form the oxides.³¹ In this paper, we discuss the photofragmentation mechanisms for $\text{Ln}(\text{hfac})_3$, $\text{Ln}(\text{fod})_3$, and $\text{Ln}(\text{hfac})_3\text{diglyme}$ and the propensity for gas-phase formation of lanthanide fluorides.

We also further illustrate the strength of photoionization time-of-flight mass spectrometry (PI-TOF-MS) as a tool for investigating photochemical mechanisms in fragmentation of metal-organic LCVD precursors. There has been considerable effort directed toward understanding more general MOCVD fragmentation mechanisms in the past decade, including, for example, monitoring in situ luminescence³² and infrared absorbance (FTIR),^{33,34} and trapping volatile intermediates³⁴ and byproducts¹ of the deposition and analyzing them with electron impact ionization (EI) mass spectrometry. Except for two early publications,^{35,36} it is only recently that the wealth of mechanistic detail available through PI-TOF-MS has become clear.^{3,26–28} The fluorinated lanthanide-based MOCVD precursors discussed in this work provide another convincing example of the potential for this technique.

- (30) Malandrino, G.; Fragalà, I. L. *Coord. Chem. Rev.* **2006**, *250*, 1605.
 (31) Nigro, R. L.; Toro, R.; Malandrino, G.; Fragalà, I. L. *Chem. Mater.* **2003**, *15*, 1434.
 (32) Talaga, D. S.; Hanna, S. D.; Zink, J. I. *Inorg. Chem.* **1998**, *37*, 2880.
 (33) Condorelli, G. G.; Baeri, A.; Fragalà, I. L. *Chem. Mater.* **2002**, *14*, 4307.
 (34) Jiang, Y.; Mingfei, L.; Wang, Y.; Song, H.; Gao, J.; Meng, G. *J. Phys. Chem.* **2006**, *110*, 13479.
 (35) Morris, J. B.; Johnson, M. V. *J. Phys. Chem.* **1985**, *89*, 5399.
 (36) Bartz, J. A.; Galloway, D. B.; Huey, L. G.; Glenwinkel-Meyer, T.; Crim, F. F. *J. Phys. Chem.* **1993**, *97*, 11249.

Experimental Section

Sample Preparation and Characterization. $\text{EuCl}_3 \cdot 6\text{H}_2\text{O}$ (99.9%) was purchased from GFS Chemicals. $\text{Tb}(\text{NO}_3)_3 \cdot 6\text{H}_2\text{O}$ (99.9%), $\text{Pr}(\text{NO}_3)_3 \cdot 6\text{H}_2\text{O}$ (99.9%), $\text{Gd}(\text{NO}_3)_3 \cdot 6\text{H}_2\text{O}$ (99.9%), Eu_2O_3 (99.9%), and Gd_2O_3 (99.9%) were obtained from Sigma-Aldrich. The ligands, 1,1,1,5,5,5-hexafluoro-2,4-pentanedione (Hhfac, 98%) and diethylene glycol dimethyl ether (diglyme) were purchased from Sigma-Aldrich. The precursor molecules, $\text{Eu}(\text{fod})_3 \cdot \text{H}_2\text{O}$ and $\text{Pr}(\text{fod})_3 \cdot \text{H}_2\text{O}$, were also purchased from Sigma-Aldrich and used as received.

$\text{Ln}(\text{hfac})_3$ was prepared as in ref 23. Briefly, 1.0 mmol of the lanthanide salt, $\text{LnCl}_3 \cdot 6\text{H}_2\text{O}$ or $\text{Ln}(\text{NO}_3)_3 \cdot 6\text{H}_2\text{O}$, was dissolved in 5 mL of H_2O and placed in a separatory funnel. An ethereal solution of NH_4hfac was prepared by dissolving 3.0 mmol of Hhfac in 100 mL of ethyl ether and adding 3 mmol of NH_4OH (0.18 g, 30 w/w %) to neutralize. The aqueous lanthanide solution was extracted with two aliquots (50 mL each) of the NH_4hfac /ether solution. The organic phase, which then contained the $\text{Ln}(\text{hfac})_3$ product, was washed with 10 mL H_2O and dried over Na_2SO_4 . The ether was evaporated slowly at room temperature leaving a solid powder of $\text{Ln}(\text{hfac})_3 \cdot 2\text{H}_2\text{O}$.

Europium(III) and gadolinium(III) polyether adducts, $\text{Ln}(\text{hfac})_3\text{diglyme}$, were prepared from the oxides using a method proposed by Fragalà et al.³⁷ Eu_2O_3 or Gd_2O_3 (0.5 mmol) was suspended in 50 mL of *n*-hexane, with 1 equiv of diglyme ($\text{CH}_3\text{O}(\text{C}_2\text{H}_4\text{O})_2\text{CH}_3$, 0.134 g, 1.0 mmol). After stirring for 10 min, Hhfac (0.624 g, 3 mmol) was added to the solution. The mixture was then refluxed at 69 °C overnight. The warm solution was filtered to remove residual solid. Crystals (~60% yield) were obtained after slow evaporation of the solvent. The structure was confirmed by single-crystal X-ray diffraction.

The method described above, however, does not work well for the praseodymium analog. A more recent method by Fragalà et al.³⁸ starts with the nitrate salts. For the current study, a 250 mL round-bottom flask was charged with $\text{Pr}(\text{NO}_3)_3 \cdot 6\text{H}_2\text{O}$ (0.435 g, 1.0 mmol), suspended in 100 mL dichloromethane. Diglyme (0.134 g, 1.0 mmol) and NaOH pellets (0.12 g, 3.0 mmol) were added to the suspension. The mixture was stirred vigorously for 10 min. Then Hhfac (0.624 g, 3.0 mmol) was added and the mixture was refluxed at 55 °C overnight. The hot solution was filtered, and the crystalline product was collected after slow evaporation of the solvent. The reaction yield was 85%. The melting point of the crude product was 335–340 K. The adduct, $\text{Pr}(\text{hfac})_3\text{diglyme}$ was tested for thermal stability under sublimation in vacuo; the sublimed product gave melting point and direct-insertion electron-impact mass spectrometry results similar to the presublimed product. Single-crystal X-ray diffraction confirmed the structure previously reported in ref 38.

Photoionization Time-of-Flight (PI-TOF) Mass Spectrometry. The molecular source was provided by the metal–organic precursor seeded in He gas. The He and precursor mixture was introduced into the ionization region through a General Valve series-9 high-speed solenoid valve (0.5 mm orifice) with ~200 μs pulses at 10 Hz and an adjustable He backing pressure of 30–160 kPa. The molecular beam source assembly, which included a reservoir of solid precursor, was heated to approximately 55 °C for $\text{Ln}(\text{hfac})_3\text{diglyme}$ and to 110 °C for $\text{Ln}(\text{hfac})_3$

and $\text{Ln}(\text{fod})_3$. The relatively high vapor pressure of these CVD precursors at low temperatures suggests that in loading the samples or in handling them in instances that require the containers be open to the atmosphere, the work should be done in a hood with appropriate ventilation to prevent inhalation and consequent heavy metal poisoning.

The ionization region for the mass spectrometer is centered in the source chamber, a six-way stainless steel cross with 8-in. flanges, evacuated through the bottom flange by a 6-in. diffusion pump. The bottom flange is fitted with a liquid- N_2 baffle to reduce pump oil in the source chamber. Repeller, extraction, and accelerator plate voltages in the vertically aligned lens stack were set to 3, 2, and 0 kV respectively. Four horizontal steering plates, located just above the ion source and lens stack, were adjusted between 300 and –300 V to optimize the ion signal. The 1-m long flight tube extends vertically from the top of the chamber. At the top of the flight tube is a 40 mm microchannel triple-plate detector assembly. The lens stack, flight-tube, and detector were purchased from Jordan TOF Products, Inc. The detector current was measured using a Tektronix TDS2022 200-MHz dual-channel digital oscilloscope using 50 or 300 Ω termination. The flight tube is additionally pumped using a Varian V300HT 6-in. air-cooled turbomolecular pump. The lens stack, which extends down from the flight tube, into the source chamber, is provided with a shroud with open ports for entry and exit of the molecular source and for entry and exit of the photoionization laser. This shroud allows for differential pumping and reduced pressure in the flight tube relative to the source chamber. The entry port for the molecular source is equipped with a removable skimmer which further improves the differential pumping but reduces the overall ion signal. The shroud, without the skimmer, was employed for the experiments described herein.

The molecular source, described above, enters the ionization region in the horizontal plane between the repeller plate and extraction grid at 90° relative to the photoionization laser beam, which also lies in the horizontal plane. The photoionization laser is a Continuum Surelite II Nd:YAG operating at 266, 355, or 532 nm. Alternatively, the YAG pumps an optical parametric oscillator (Continuum SLOPO) that operates between 410 and 720 nm, which subsequently serves for photoionization. In both cases, the laser is focused into the center of the ionization region using a 12-in focal length, fused silica lens.

Results and Discussion

For the $\text{Ln}(\text{hfac})_3$ and $\text{Ln}(\text{fod})_3$ precursors, photofragmentation experiments were conducted using the 266, 355, and 532 nm harmonics from a Nd:YAG laser. The dominant products observed for photofragmentation and ionization at all wavelengths and all laser powers were Ln^{2+} , Ln^+ , LnF^+ , and LnF_2^+ , in addition to low-mass fragments attributed to the ligand. As an example, Figure 2 shows the photoionization mass spectra for $\text{Eu}(\text{hfac})_3$ and $\text{Eu}(\text{fod})_3$ using 532 nm and pulse energies of approximately 200 mJ (~ 10^{10} W/cm²). The fragmentation products shown in Figure 2 stand in sharp contrast to those reported for $\text{Ln}(\text{thd})_3$, which showed significant oxide, LnO^+ formation.^{26–28} The oxygen coordination in all of the β -diketonate complexes, $\text{Ln}(\text{thd})_3$, $\text{Ln}(\text{hfac})_3$, and $\text{Ln}(\text{fod})_3$ is similar, but the fluorinated ligands appear to disfavor oxide formation. A weak metal oxide signal was observed for $\text{Pr}(\text{hfac})_3$ and for $\text{Pr}(\text{fod})_3$ at 355 nm,

(37) Malandrino, G.; Benelli, C.; Castelli, F.; Fragalà, I. L. *Chem. Mater.* **1998**, *10*, 3434.

(38) Nigro, R. L.; Toro, R. G.; Malandrino, G.; Fragalà, I. L.; Rossi, P.; Dapporto, P. *J. Electrochem. Soc.* **2004**, *151*, F206.

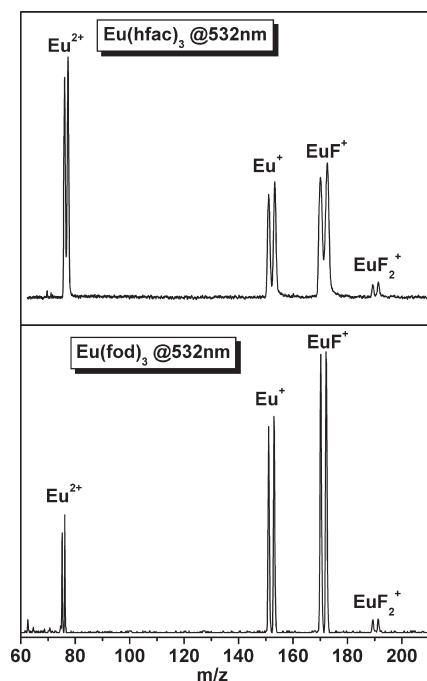
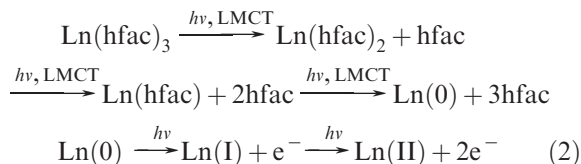


Figure 2. PI-TOF mass spectra for $\text{Eu}(\text{hfac})_3$ (top) and $\text{Eu}(\text{fod})_3$ (bottom) at 532 nm (200 mJ/pulse). The dominant ions are Eu^{2+} , Eu^+ , and EuF^+ , together with the much weaker feature for EuF_2^+ .

as shown in Figures 3 and 4, respectively, but no metal oxide was observed for the europium, terbium (not shown), or gadolinium analogues. As can also be seen in Figure 3, the relative propensity for formation of the LnF^+ and LnF_2^+ products is metal dependent, with $\text{Eu}(\text{hfac})_3$ and $\text{Eu}(\text{fod})_3$ showing very low EuF_2^+ yield. None of the metals showed formation of any LnF_3^+ .

Production of the bare metal ions, Ln^+ and Ln^{2+} , likely follows the same mechanism invoked for bare metal production from $\text{Ln}(\text{thd})_3$, i.e., sequential dissociation of intact neutral ligands following photoexcitation to repulsive regions of a ligand-to-metal charge-transfer state, as illustrated in eq 2.



In most of the steps for the mechanism shown in eq 2, the symbol $h\nu$ over the arrows represents a multiphoton process.

The observed metal fluoride production is consistent with the earlier results of Zink et al. who observed the spectroscopic signature of neutral CrF following $\text{Cr}(\text{hfac})_3$ photolysis.³² Morris and Johnson also noted MF^+ production in the multiphoton ionization of $\text{Cu}(\text{hfac})_3$ and $\text{Fe}(\text{hfac})_3$.³⁵ Zink³² proposed a unimolecular reaction that was initiated by rotation of the $\text{C}_\alpha\text{--C}(\text{O})$ bond, bringing the CF_3 group into proximity with the metal and allowing metal abstraction of fluorine. In the proposed mechanism, breaking of the metal–oxygen bond, which allows the $\text{C}_\alpha\text{--C}(\text{O})$ bond rotation, is initiated

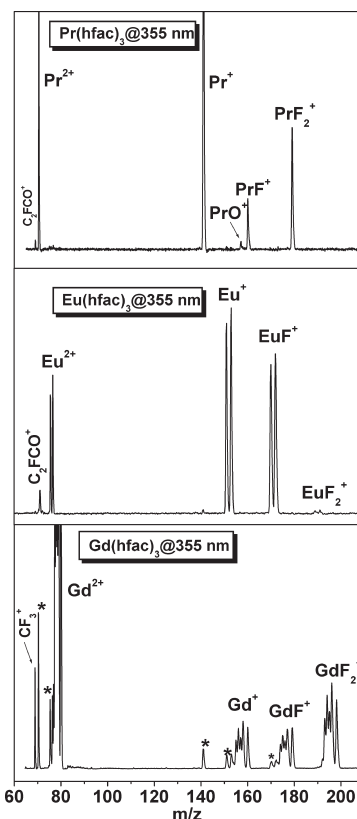


Figure 3. Photoionization TOF-mass spectra of $\text{Pr}(\text{hfac})_3$, $\text{Eu}(\text{hfac})_3$, and $\text{Gd}(\text{hfac})_3$ (from top to bottom) at 355 nm (~ 110 mJ/pulse). The dominant ions are Ln^{2+} , Ln^+ , LnF^+ , and LnF_2^+ . The asterisks in the bottom panel mark contamination from Pr and Eu.

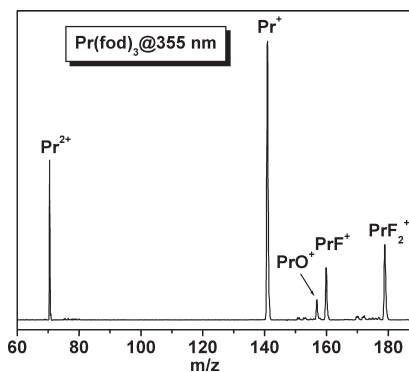
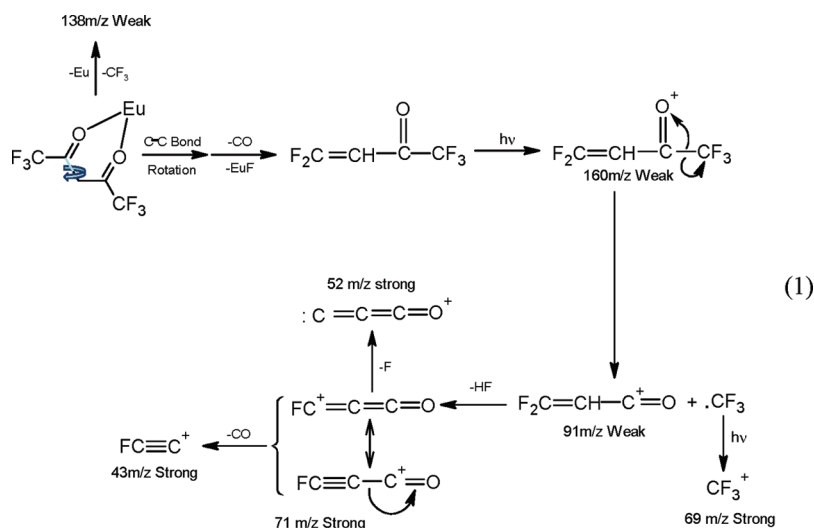


Figure 4. Photoionization TOF-mass spectrum of $\text{Pr}(\text{fod})_3$ at 355 nm (~ 110 mJ/pulse). As for $\text{Pr}(\text{hfac})_3$, and in contrast to the Gd, Eu, and Tb analogs, the oxide (PrO^+) ion is observed.

through ligand-to-metal charge-transfer. The net effect of an LMCT electron and a fluorine is fluoride transfer to the metal and ejection of neutral fragments. An analogous bond rotation is illustrated for $\text{Eu}(\text{hfac})_3$ in the first structure given in Scheme 1.

A similar rotation was proposed by Condorelli et al. as a reasonable mechanism to explain the production of SrF_2 from the MOCVD of $\text{Sr}(\text{hfac})_2$ tetraglyme.³³ Pollard et al. further proposed that the metal fluoride formation would be accompanied by elimination of CO as illustrated in the eq 3 shown below.¹



Scheme 1. Hfac Ligand Rotation and Fragmentation^a

^aThe hfac ligand fragments as it dissociates from the Eu ion leaving EuF, CO, and CF₂CHC(O)CF₃. Upon photoionization, this latter fragment produces strong daughter fragments at $m/z = 43, 52, 71,$ and 69 . The weak/strong annotation refers to ion signal strength in the Eu(hfac)₃ photoionization mass spectrum. The first step, with double consecutive arrows to the right, shows rotation about the C_α-C(O) bond, bringing the CF₃ group into proximity to the metal. A fluorine is transferred to the metal and the remaining CF₂ group forms a new bond with the α-carbon, which lies between the two β-carbonyls. This results in elimination of the CO group, which was rotated away from the metal, and of the remaining CF₂=CHC(O)CF₃. Both of these fragments may be photoionized and are observed in the mass spectrum. However, upon photoionization, the latter fragment forms a radical cation that is unstable to CF₃ elimination. The resulting closed-shell cation at $m/z = 91$ is also observed but is subject to further fragmentation with HF elimination and formation of the resonance-stabilized, [FC=C=C=O]⁺, which is strongly represented in the mass spectrum at $m/z = 71$. This species is subject to further fragmentation, eliminating CO to produce FC₂⁺ at $m/z = 43$ or to elimination of fluorine to produce the stable carbene radical C₃O⁺ at $m/z = 52$. This latter ion has been implicated in the chemistry of interstellar dust.³⁹

We observed a distinct feature characteristic of CO⁺, at $m/z = 28$, in the 266 nm photofragmentation mass spectra of Ln(hfac)₃ and Ln(fod)₃, which is absent in the Ln(thd)₃ spectra. Interference by atmospheric N₂ was rejected on the basis of the consistent presence of the signal for fluorinated precursors and absence for Ln(thd)₃. The basis for rejection of atmospheric N₂⁺ was further supported by the absence of either O₂⁺ or H₂O⁺ signal, although both O₂ and H₂O are more easily ionized than N₂ in air samples using the laser wavelength and power employed in our experiments. However, significant CO⁺ signal was also observed in the photoionization mass spectrum of the uncoordinated Hhfac ligand. Thus, the observation of CO⁺ alone is insufficient to support the proposed mechanism in eq 3.

The companion fragment from CO elimination, CF₂=CHC(O)CF₃, with a mass of 160 amu, is difficult to observe, perhaps because it is subject to further fragmentation following ionization. Compounding the difficulty, the 160 mass channel also suffers from interference from ¹⁶⁰Gd⁺, ¹⁴¹PrF⁺, or ¹⁵⁹Tb⁺. A weak signal at 160 was observed for Eu(hfac)₃ photofragmentation in the window between Eu⁺ and EuF⁺. However, a set of much stronger peaks, which are consistent with the CF₂=CHC(O)CF₃⁺ fragmentation mechanism illustrated in Scheme 1 are observed at lower m/z . According to this mechanism, CF₂=CHC(O)CF₃⁺ fragments to produce species at $m/z = 43, 52, 69, 71,$ and 91 . The annotations in Scheme 1 regarding signal strength of the m/z fragments refer to the mass spectrum of Eu(hfac)₃ shown in Figure 5. Referring to Figure 5, the features at $m/z = 71, 52,$ and 43 are consistently present in the Ln(hfac)₃ spectra but are essentially absent in the Hhfac and Ln(thd)₃ spectra.

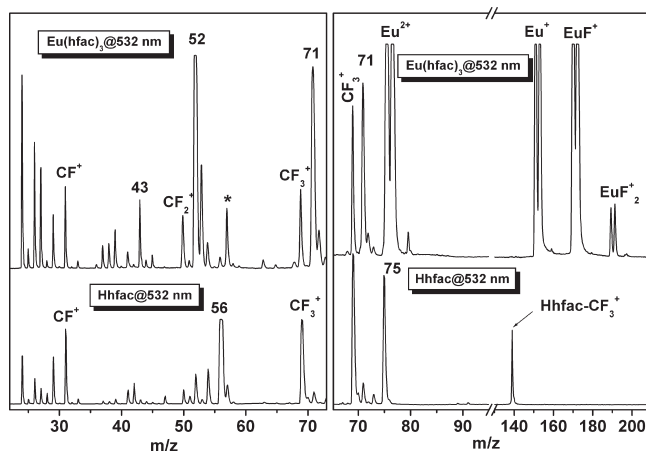


Figure 5. Photoionization (532 nm) TOF-mass spectra of Eu(hfac)₃ and Hhfac. The peaks at $m/z = 43, 52,$ and 71 are characteristic fragments from Eu(hfac)₃, and are weak or absent in the spectrum of Hhfac. The asterisk at $m/z = 57$ indicates background signal present when the pulsed valve is closed. Flat-top features at 52 and 56 and for the metal containing species represent mass channels for which ion intensity is off-scale on the oscilloscope.

Weak features at $m/z = 160$ and 91 are also observed in the Ln(hfac)₃ spectra under optimized conditions. The feature at $m/z = 69$, assigned to CF₃⁺, is strong in the spectra of both Ln(hfac)₃ and Hhfac.

The observation of all charged species predicted in the proposed photofragmentation mechanism, in conjunction with the unique association of the strong features at $m/z = 71, 52,$ and 43 with the Ln(hfac)₃ spectrum, provides a convincing argument in support of the mechanism in eq 3. As discussed below, however, the fluorination of the metal ion may not occur until after the first hfac ligand has dissociated.

In earlier work,^{27,28} high-mass fragments, e.g., Ln(thd)₃⁺, Ln(thd)₂⁺, and Ln(thd)⁺ had proven useful in elucidating the photofragmentation mechanism for Ln(thd)₃. However, the spectra for Ln(hfac)₃ and Ln(fod)₃ show no signal for the parent ion, and in fact, show no metal-containing mass fragments heavier than LnF₂⁺. Observation of these fragments may have helped elucidate whether metal fluorination occurs via a step-by-step mechanism, with one fluoride being attached per ligand, as might be expected from eq 3 above. If this were the case, the high-mass fragmentation pattern may also have indicated which two of the three ligands are involved in metal fluorination. The reason for the absence of these features is not entirely clear, but hfac⁻ and fod⁻ may lack a favorable steric factor which could slow dissociation, making the intermediates more easily observable. The thd⁻ ligand, for example, for which high-mass fragments are observed, is more bulky than either hfac⁻ or fod⁻. Furthermore, if we add a bulky ether adduct to the Ln(hfac)₃ complexes, e.g., Ln(hfac)₃diglyme, the high-mass fragments become quite evident.

In all cases, observation of the high mass fragments required reducing the laser power ($\sim 10^9$ W/cm²), working at low backing pressures (< 100 kPa He), and optimizing the horizontal steering plates with settings different from those which were optimal for the LnF_x⁺ fragments. The high-mass fragments all show relatively broad peaks with poor mass resolution, presumably as a result of several factors, including (1) the isotopic distribution of the metal, (2) the high carbon content and consequent ¹³C representation, and (3) the long flight time (25–45 μs), resulting in collisional broadening. The heavy fragments, with their long flight times, suffer numerous He collisions during their transit, impacting the vertical velocity and resulting in a spread in the time-of-flight. An additional factor may arise from the kinetic energy released accompanying ligand dissociation. Asymmetric broadening, skewed toward high mass, can also result if the observed ion results from slow postionization fragmentation of a heavier ion. In summary, the origins of the broadening may be several. The problem is not entirely resolved and will be the subject of future work. Similar phenomena have been noted in previous work on photoionization mass spectrometry of metal β-diketonates.^{27,28,35,36}

Figure 6 shows the PI-TOF spectrum for Pr(hfac)₃diglyme using 532 and 266 nm excitation. It was previously argued for Ln(thd)₃ that the majority of the high-mass fragments represented intermediates, isolated in a stepwise fragmentation.^{27,28} Accepting this premise, several points become clear regarding the interpretation of the Pr(hfac)₃diglyme spectrum in Figure 6. First, the neutral diglyme molecule is less labile under photolysis than the anionic hfac⁻ ligand. The majority of fragments retain the diglyme even as the hfac ligands dissociate from the metal center. This is consistent with the mechanism of ligand–metal dissociation involving ligand-to-metal

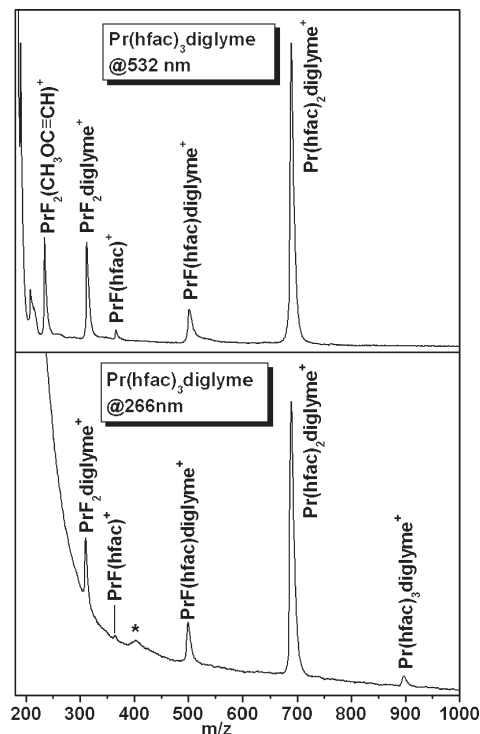


Figure 6. Photoionization TOF-mass spectrum of Pr(hfac)₃diglyme at 532 and 266 nm (~ 60 mJ/pulse). The high-mass fragments reveal details of the photofragmentation mechanism.

charge-transfer, as outlined for Ln(thd)₃ in the Introduction. Photoexcitation of the complex into the LMCT state significantly weakens the ionic metal-(β-diketonate) bond and prepares the complex in a state that is repulsive along the metal–hfac distance coordinate. Bonding of the neutral ether to the metal, though initially much weaker than the metal–hfac bonding, would be much less affected by charge transfer from hfac⁻, and the neutral ether itself would be unlikely to act as a donor in LMCT.

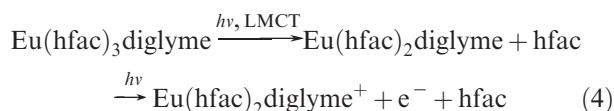
Second, it appears that the first ligand dissociates cleanly, leaving Pr(hfac)₂diglyme. However, the next highest mass is PrF(hfac)diglyme, indicating that the second ligand attached a fluoride to the metal prior to dissociation. Similarly, the strong PrF₂diglyme feature indicates that the third ligand also attaches a fluoride to the metal prior to dissociation. PrF₂⁺ is a strong feature at the low *m/z* portion of both spectra for which the signal strength is offscale.

The PI-TOF spectra of Eu(hfac)₃diglyme and Gd(hfac)₃diglyme shown in Figure 7 exhibit features similar to those discussed above for Pr(hfac)₃diglyme, and the spectra can be interpreted in an analogous manner. Binding of the diglyme is robust, and the first hfac ligand dissociates with no fluoride attachment.

Of all the Ln(hfac)₃diglyme compounds studied, the PI-TOF of Eu(hfac)₃diglyme, shown in Figure 8, yielded the greatest mechanistic detail. This spectrum was acquired using low-power (~ 1 mJ/pulse) photoionization at 412 nm. The parent ion, Eu(hfac)₃diglyme⁺, is clearly observable. The adjacent lower-mass feature, Eu(hfac)₂diglyme⁺, results from loss of an intact hfac ligand from Eu(hfac)₃diglyme.

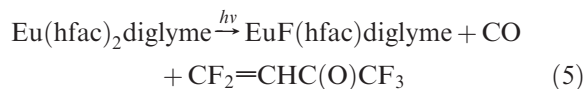
(39) Petrie, S.; Bettens, R. P. A.; Freeman, C. G.; McEwan, M. J. *J. Phys. Chem.* **1993**, *97*, 13673.

We attribute this step to LMCT-mediated dissociation of neutral species and subsequent photoionization of $\text{Eu}(\text{hfac})_2\text{diglyme}$.

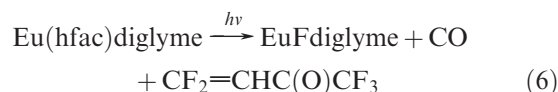


The next mass fragments are $\text{Eu}(\text{hfac})\text{diglyme}^+$ and $\text{EuF}(\text{hfac})\text{diglyme}^+$, with the former showing three times the intensity of the latter. The $\text{Eu}(\text{hfac})\text{diglyme}^+$ is thought to arise from the dissociation of a second intact, neutral hfac ligand, again mediated by a LMCT state. The $\text{EuF}(\text{hfac})\text{diglyme}^+$ is thought to arise from

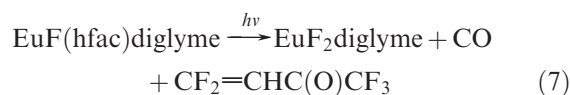
the following mechanism:



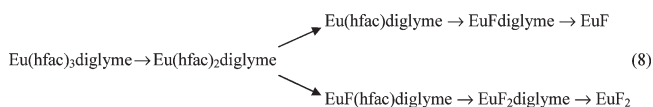
which is similar to the process outlined in eq 3. At lower values of m/z , EuFdiglyme^+ and $\text{EuF}_2\text{diglyme}^+$ are observed in the same 3:1 ratio as observed for $\text{Eu}(\text{hfac})\text{diglyme}^+$ to $\text{EuF}(\text{hfac})\text{diglyme}^+$. The obvious interpretation is that EuFdiglyme^+ and $\text{EuF}_2\text{diglyme}^+$ are formed from $\text{Eu}(\text{hfac})\text{diglyme}^+$ and $\text{EuF}(\text{hfac})\text{diglyme}^+$, respectively, via ligand dissociation following a loss of one fluoride to the metal, as illustrated below.



or



Given the similar ratios of $\text{Eu}(\text{hfac})\text{diglyme}^+$ to $\text{EuF}(\text{hfac})\text{diglyme}^+$, EuFdiglyme^+ to $\text{EuF}_2\text{diglyme}^+$, and EuF^+ to EuF_2^+ , it is reasonable to hypothesize that the EuF^+ to EuF_2^+ ratio is determined by the branching ratio at the second ligand dissociation step and to propose an overall mechanism given by



However, the 3:1 ratio observed in the mass spectrum is not a quantitative measure of the branching ratio shown above, since the multiphoton ionization yield is different for species in the two reaction pathways. Ionization of the three species in the EuF path is favored by the lower $\text{Eu}(\text{I}) \rightarrow \text{Eu}(\text{II})$ ionization potential as compared to the $\text{Eu}(\text{II}) \rightarrow \text{Eu}(\text{III})$ ionization potential which is relevant to ionization of the species in the EuF_2 path (11 vs 25 eV). This difference is offset to some extent by the extra charge

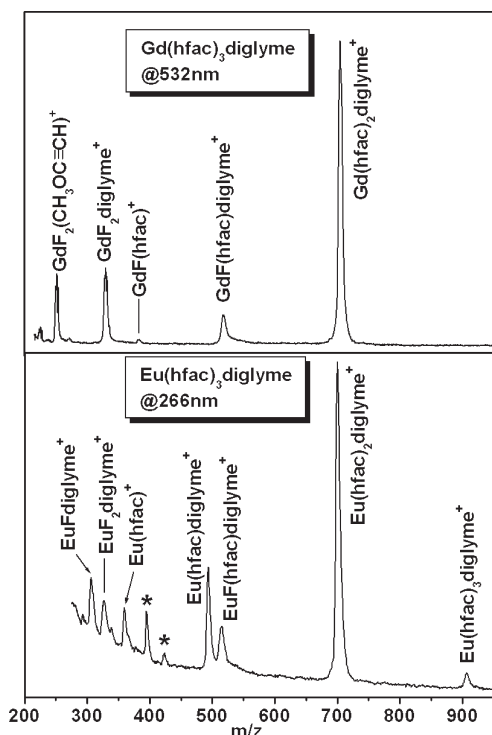


Figure 7. Photoionization TOF-mass spectra of $\text{Gd}(\text{hfac})_3\text{diglyme}$ and $\text{Eu}(\text{hfac})_3\text{diglyme}$ at 532 and 266 nm, respectively. These spectra show a fragmentation pattern analogous to that seen for $\text{Pr}(\text{hfac})_3\text{diglyme}$ except in that the Eu species shows a parallel path in which the second hfac ligand dissociates without depositing fluoride. The asterisks in the bottom panel show background interference.

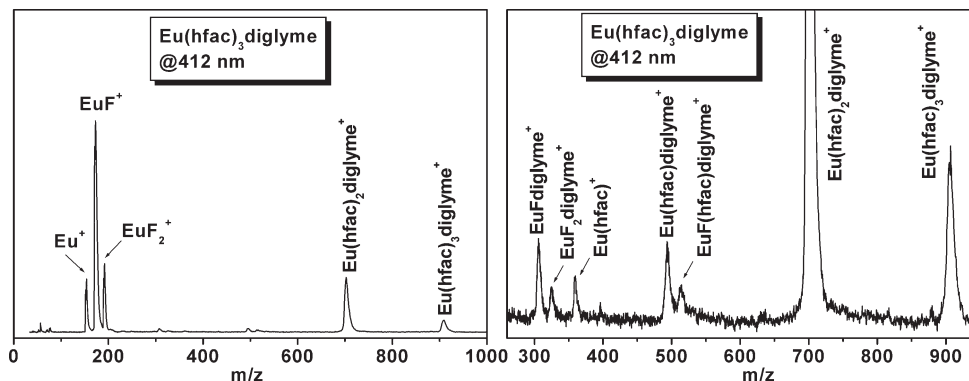


Figure 8. Photoionization TOF-mass spectrum of $\text{Eu}(\text{hfac})_3\text{diglyme}$ at 412 nm (~ 1 mJ/pulse). The right panel shows an expanded scale, revealing the parallel paths to EuF and EuF_2 .

stabilization provided by the additional fluoride ion in the EuF_2 path. However, the net effect is that the relative ion yield for the species in the EuF pathway should exceed that of the EuF_2 pathway. Therefore, the branching ratio of the EuF to the EuF_2 pathways is likely less than 3:1.

$\text{Gd}(\text{hfac})_3\text{diglyme}$ and $\text{Pr}(\text{hfac})_3\text{diglyme}$ appear to have a greater affinity for the LnF_2 pathway relative to $\text{Eu}(\text{hfac})_3\text{diglyme}$. The LnF feature was weaker than LnF_2 in the mass spectrum, and the LnF path intermediates $\text{Ln}(\text{hfac})\text{diglyme}^+$ and LnFdiglyme^+ were not detected for gadolinium and praseodymium. The end products, GdF^+ and PrF^+ , were both observed; however, these features are not as strongly represented as EuF^+ .

Conclusion

In laser-assisted chemical vapor deposition using metal–organic precursors, the nature of deposited materials is strongly influenced by unimolecular gas-phase reactions. In this work, the reaction mechanisms for several lanthanide-based precursors with fluorinated β -diketonate ligands have been elucidated using photoionization time-of-flight mass spectrometry. The dissociation of $\text{Ln}(\text{hfac})_3\text{diglyme}$ leads to dominant production of gas-phase metal fluoride and appears to proceed with intact loss of the first ligand followed by sequential loss of the second and third ligands, each with the potential for fragmenting and attaching a single fluoride to the metal center. The fluorination process is in competition with production of bare metal Ln^0 which is thought to proceed through a mechanism of sequential dissociation of intact ligands, mediated by photoexcitation to dissociative regions of LMCT states.

The mass spectra of the photoproducts are consistent with individual fluorination steps analogous to that proposed by Zink³² and later elaborated on by Pollard et al.,¹ involving (1) a unimolecular ligand-bond rotation, bringing the fluorine into close proximity to the metal, (2) fluoride transfer to the metal, and (3) elimination of CO and a neutral $\text{CF}_2=\text{CHC}(\text{O})\text{CF}_3$ fragment.

The results suggest that to avoid metal fluoride formation, optimal ligand design must restrict the critical $\text{C}_\alpha\text{--C}(\text{O})$ bond rotation or, alternatively, selectively eliminate fluorine substitution on the carbon adjacent to the carbonyl. For example, $\text{CF}_3\text{CF}_2\text{CH}_2\text{C}(\text{O})\text{CH}_2\text{C}(\text{O})\text{C}(\text{CH}_3)_3$ might be tried as an alternative to Hfod . The robust nature of the binding of the diglyme adduct also suggests that adducts might be chosen not only to enhance mass transport properties but also to engage in final-step chemistry, augmenting the frequently used coprecursor strategy. That is, the metal–adduct complex may be induced to react after dissociation of the β -diketonate ligands. For the precursors in this study, the fluorination step appears to disfavor metal oxide formation and may also deter potential metal–adduct reactions. Thus, elimination of metal fluoride formation might promote metal–adduct chemistry.

The current study suggests several strategies for favorable engineering of precursor chemistry and further supports photoionization mass spectrometry as a powerful tool in determining the photodecomposition mechanisms for newly developed precursors.

Acknowledgment. This material is based upon work supported by the National Science Foundation/EPSCoR Grant No. 0554609 and by the State of South Dakota, Governor's Office of Economic Development.